Emerging Science Innovation, vol. 4, 2024, pp. 17-32

Locomotion Control of a Bipedal Wheeled Robot Using Virtual Model Control and Linear Quadratic Regulator Techniques

Dan-Dan Liu[1], Wei Wang[1,*]

[1]School of Electrical Engineering, Yancheng Institute of Technology, Yancheng, Jiangsu, China

Received 26 June 2024; received in revised form 24 August 2024; accepted 26 August 2024

DOI: https://doi.org/10.46604/emsi.2024.13923

Abstract

This paper aims to develop a balance control technique and investigates its impact on the stability and disturbance rejection capability of a bipedal wheeled robot. The bipedal wheeled robot is equivalent to a wheeled inverted pendulum nonlinear model with a legs-airframe centroid variable rod. The nonlinear model is linearized and decoupled into two subsystems: straight-line control using linear-quadratic regulator (LQR) for balance and speed, and steering control employing proportional integral derivative (PID). Height control adjusts the virtual force with PID-Feedforward, while hip torque is determined by virtual model control (VMC). MATLAB simulation confirms effective control of height, linear motion, and steering, with decoupling enhancing steering performance.

Keywords: bipedal wheeled robot, wheeled inverted pendulum model, linear quadratic regulator (LQR), proportional integral derivative, virtual model control (VMC)

1. Introduction

With the rapid development of science and technology, robotics has penetrated nearly all aspects of daily life and industrial production. As a significant category of robots, mobile robots have wide-ranging applications across terrestrial, aerial, underwater, and even extraterrestrial environments. The existing motion mechanisms of mobile robots can be broadly categorized into two main areas: wheel-based systems [1-3] and leg-based systems research [4-6]. Wheeled robots are characterized by simple structures, high energy efficiency, fast mobility, and low manufacturing costs.

However, they typically have limited obstacle traversal capabilities and struggle to adapt to complex environments. On the other hand, legged robots hold greater potential for maneuverability and adaptability in complex, unstructured environments with motion patterns more akin to humans. Yet, they come with increased degrees of freedom, complex structures, and pose greater challenges in system design and control. Moreover, legged robots tend to be more expensive due to their intricate design and control systems.

Additionally, on flat surfaces, their movement speed and power consumption are generally inferior to wheeled robots. As a new type of robot [7], the wheel-legged robot has attracted widespread attention due to its design advantages of combining wheel and leg. In recent years, many new bipedal wheeled robots have emerged both domestically and internationally, such as the Ascento [8] robot developed by the Zurich team in Switzerland, and Ollie [9] from Tencent Robotics X Lab in China. Compared with traditional robots, the wheel-legged robot combines the mobility of wheeled robots with the agility of legged robots. Therefore, it offers faster and more energy-efficient movement on flat surfaces while providing better adaptability and traversal capabilities on uneven terrain. Additionally, it enables the robot to adjust its height, thereby avoiding collisions when it needs to pass through low obstacles.

* Corresponding author. E-mail address: ww2232754873@gmail.com

English language proofreader: Si-Yu-Lin

However, the high mobility of the bipedal wheeled robots also poses challenges, especially in terms of control [10,11]. Therefore, effectively achieving precise control of the bipedal wheeled robot has become a significant topic in the current research. Wang et al. [12] proposed a novel balance control technology for a bipedal wheeled robot. A linear feedback controller based on output regulation and linear quadratic regulator (LQR) adjustment methods is used to keep the robot stable on the ground without drastic forward and backward movement. To address the nonlinearities of the model and obtain a large domain of stability, a nonlinear controller based on the interconnection and damping assignment-passivity-based control (IDA-PBC) method, is introduced to control the robot in more general cases. Hsu [13] proposed an intelligent motion and balance controller (IMBC) using a fuzzy logic approach to maintain the wheeled bipedal robot's (WBR) balance while standing and moving on the ground.

The IMBC system does not require prior knowledge of system dynamics, as the controller parameters are adjusted based on qualitative aspects of human knowledge. Cao [14] developed a model prediction controller (MPC) with input constraints to maintain the robot's balance. In order to deal with unmodeled dynamics and external disturbances, an extended state observer (ESO) is designed to enhance the robustness of the controller. The proposed control method can ensure the balance of the robot and has satisfactory adaptability to external disturbances. Zhang et al. [15] adopted a combination of whole-body control (WBC) and a learning-based adaptive technique for the Ollie robot, which effectively improves the sensitivity of the system.

For nonlinear complex systems, traditional control algorithms often exhibit performance limitations, hindering precise control. Therefore, advanced optimization techniques are needed to optimize traditional algorithms. Taking the PID algorithm as an example, Kanungo [16] introduced the novel wavelet-based fuzzy-adaptive hybrid bat-vulture PID (WFAHBVPID) controller for controlling brushless direct current (BLDC) motor acceleration. The proposed controller achieves low error rates of 0.002% and 0.02% under optimized and non-optimized conditions, respectively.

However, compared to other models, the computational time increases by 66.14%. To mitigate noise effects on the direct current (DC) motor, Kanungo [17] also proposed a multi-resolution proportional integral derivative (MRPID) controller, leveraging wavelet multi-resolution properties to enhance PID controller performance. The performance of MRPID, fractional order PID (FOPID), and traditional PID controllers is compared under noise conditions to demonstrate superior results in transient response and disturbance rejection achieved with the MRPID controller. Itaborahy Filho [18] analyzed several variants of metaheuristic techniques to find generic algorithm proportional integral derivative (GAPID) control parameters for a Buck converter.

The GAPID control of the Buck converter is implemented using the MATLAB/Simulink platform, and experiments with 10 different variants of the genetic algorithm (GA), differential evolution (DE), and particle swarm optimization (PSO) algorithms reveal that variants generally implemented with PSO and DE exhibit the highest fitness. Shao [19] proposed a fuzzy adaptive particle swarm optimization-proportional integral derivative (PSO-PID) pitch control strategy, where PID parameters are initially optimized by PSO and adaptively adjusted by a fuzzy controller.

Through simulation verification, the fuzzy adaptive PSO-PID effectively reduces errors in wind turbine rotational speed and output power compared to fuzzy PID and PID alone. Advanced optimization techniques can generally improve the performance of traditional algorithms. This study aims to investigate the effects of employing the LQR and VMC algorithms on the stability and disturbance rejection capabilities of a two-wheeled legged robot, enabling precise control of the leg height, and to compare the impact of decoupling on system performance. Compared to using a general LQR algorithm to control a bipedal wheeled robot, the LQR algorithm approach presented in this study allows for more precise control of the robot by adjusting the gain K according to the leg length.

2. Modeling of a Bipedal Wheeled Robot

2.1. Model of a bipedal wheeled robot

Fig. 1 shows a bipedal wheeled robot model consisting of two wheels, a body, and two legs, connected by five swivel joints on each side. The structure of the robot's leg is composed of four connecting rods, including the frame. The hip actuator consists of two servos, and the wheel actuator consists of two motors. In the MATLAB simulation environment, the body and legs of the bipedal wheeled robot are regarded as ideal rigid bodies. The centroid of each part is located at the geometric center of each rigid body, and the left and right sides are assumed to be perfectly symmetrical.

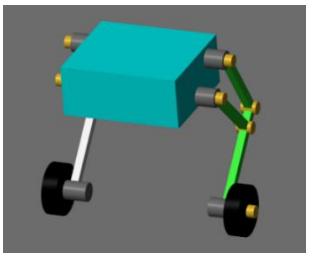

Fig. 1 Model of a bipedal wheeled robot

2.2. Equivalent handstand pendulum model

In the process of modeling the bipedal wheeled robot, the motion of the robot is broken down into wheel motion and leg motion, and the control object can be regarded as a wheeled inverted pendulum model with a legs-airframe centroid variable rod, as shown in Fig. 2.

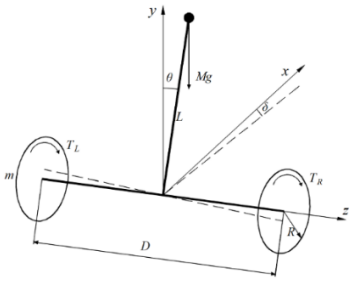

Fig. 2 Wheeled inverted pendulum model

Searching for existing design models or studying a newly available design model with required specifications and establishing the topological structure of these models is the first step of the methodology. The goal of this step is to select some models mentioned above to research their equivalent mechanism skeleton and kinematic chain in order to develop new designs.

2.2.1. Legs-airframe centroid calculation

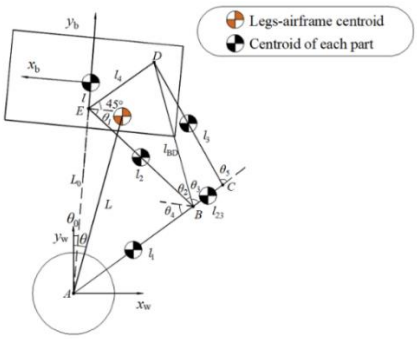

Fig. 3 Schematic diagram of the distribution of the centroid of the legs-airframe

Due to the pitch angle of the bipedal wheeled robot body, the angle of each joint of the legs changes during movement, while the Legs-airframe centroid also changes. The position and parameters of the legs and the airframe's center of mass are shown in Fig. 3. The physical parameters of Fig. 3 are listed in Table 1 and the relationships between the parameters are presented in Eqs. (1)-(17).

Table 1 Legs-body parameters

Symbols	Definitions	Symbols	Definitions
l	The distance from the hip joint to the machine's center of mass	l_1	The length of member AB
l_2	The length of member BE	l_{23}	The length of member BC
l_3	The length of member CD	l_4	The length of member DE
L_0	The distance between the hip joint and the wheel	θ_0	The pitch angle of the body
θ_1	The angle between the hip joint and member BE in the negative direction of the $x_{\text{b-axis}}$		

$$l_{BD} = \sqrt{l_2^2 + l_4^2 - 2l_2 l_4 \cos\left(\theta_1 + \frac{\pi}{4}\right)} \tag{1}$$

$$\theta_2 = \arcsin\left(\frac{l_4 \sin\left(\theta_1 + \frac{\pi}{4}\right)}{l_{BD}}\right) \tag{2}$$

$$\theta_3 = \arccos\left(\frac{l_{BD}^2 + l_{23}^2 - l_3^2}{2 l_{BD} l_{23}}\right) \tag{3}$$

$$\theta_4 = \pi - (\theta_1 + \theta_2 + \theta_3) \tag{4}$$

$$\theta_5 = \pi - \arcsin\left(\frac{l_{BD} \sin\theta_3}{l_3}\right) \tag{5}$$

$$L_0 = l_2 \sin\theta_1 + l_1 \sin\theta_4 \tag{6}$$

$$\theta_0 = \theta_1 + \arcsin\left(\frac{l_1 \sin(\theta_1 + \theta_4)}{L_0}\right) \tag{7}$$

$$x_0 = (L_0 + l)\cos\theta_0 \tag{8}$$

$$y_0 = (L_0 + l)\sin\theta_0 \tag{9}$$

$$x_1 = \frac{1}{2} l_1 \cos(\theta_4 - \theta_0) \tag{10}$$

$$y_1 = \frac{1}{2} l_1 \sin(\theta_4 - \theta_0) \tag{11}$$

$$x_2 = l_1 \cos(\theta_4 - \theta_0) - \frac{1}{2} l_2 \cos(\theta_1 + \theta_0) \tag{12}$$

$$y_2 = l_1 \sin(\theta_4 - \theta_0) - \frac{1}{2} l_2 \sin(\theta_1 + \theta_0) \tag{13}$$

$$x_{23} = \left(l_1 + \frac{1}{2} l_{23} \right) \cos\left(\theta_4 - \theta_0 \right) \tag{14}$$

$$y_{23} = \left(l_1 + \frac{1}{2} l_{23} \right) \sin\left(\theta_4 - \theta_0 \right) \tag{15}$$

$$x_3 = \left(l_1 + l_{23} \right) \cos\left(\theta_4 - \theta_0 \right) + \frac{1}{2} l_3 \cos\left(\theta_4 - \theta_0 + \theta_5 \right) \tag{16}$$

$$y_3 = \left(l_1 + l_{23} \right) \sin\left(\theta_4 - \theta_0 \right) + \frac{1}{2} l_3 \sin\left(\theta_4 - \theta_0 + \theta_5 \right) \tag{17}$$

where (x_0, y_0) is the coordinate of the machine's center of mass, and (x_1, y_1,), (x_2, y_2,), (x_{23}, y_{23},), (x_3, y_3) are the coordinates of the centers of mass of members AB, BE, BC, and CD, respectively, relative to the wheel's center on the x_w-axis and y_w-axis.

According to Eqs. (1)-(17), the coordinates of the legs-airframe centroid can be obtained by

$$x_c = \frac{x_0 m_0 + 2x_1 m_1 + 2x_2 m_2 + 2x_{23} m_{23} + 2x_3 m_3}{m_0 + 2m_1 + 2m_2 + 2m_{23} + 2m_3} \tag{18}$$

$$y_c = \frac{y_0 m_0 + 2y_1 m_1 + 2y_2 m_2 + 2y_{23} m_{23} + 2y_3 m_3}{m_0 + 2m_1 + 2m_2 + 2m_{23} + 2m_3} \tag{19}$$

where x_c and y_c are the coordinates of the legs-airframe centroid relative to the center of the wheel on the x_w-axis and y_w-axis, the total mass, consisting of the body and members AB, BE, BC, and CD, is the sum of m_0, m_1, m_2, m_{23}, and m_3, respectively.

The angle at which the legs-airframe centroid rotate relative to the y_w-axis of the wheel's coordinate system is the virtual pitch angle θ, which can be found by

$$\theta = \arctan \frac{x_c}{y_c} \tag{20}$$

Also, the distance from the legs-airframe centroid to the midpoint between the left and right wheel centers is the centroid height L, and can be obtained by

$$L = \sqrt{x_c^2 + y_c^2} \tag{21}$$

2.2.2. Modeling of wheeled inverted pendulum dynamics

Table 2 Physical parameters of wheeled inverted pendulum

Symbols	Definitions	Symbols	Definitions
R	Drive wheel radius(m)	m	The quality of the drive wheels(kg)
L	The distance from the center of gravity to the drive wheel axle(m)	I_w	The moment of inertia of the drive wheels(N·m)
M	The total mass of the body and members(kg)	I_θ	The total moment of inertia of the body and members(N·m)
g	Gravitational acceleration(m/s^2)	I_δ	The moment of inertia at the yaw angle(N·m)
D	Drive wheel spacing(m)	θ	The angle between the body and the vertical direction(°)
T_L	Torque of the left drive wheel(N·m)	x	Horizontal displacement of a wheeled inverted pendulum(m)
T_R	Torque of the right drive wheel(N·m)	δ	The corner of the wheeled handstand pendulum(°)

The system parameters of the wheeled inverted pendulum model are listed in Table 2, and the nonlinear equations are provided as follows [20]

$$R\left(M+2m+\frac{2I_w}{R^2}\right)\ddot{x}=\left(T_L+T_R\right)-MRL\ddot{\theta}\cos\theta+ML\dot{\theta}^2\sin\theta \tag{22}$$

$$\left(I_\theta+ML^2\right)\ddot{\theta}=MgL\sin\theta-M\ddot{x}L\cos\theta-\left(T_L+T_R\right) \tag{23}$$

$$\ddot{\delta}=\frac{T_L-T_R}{R\left(mD+\frac{I_wD}{R^2}+\frac{2I_\delta}{D}\right)} \tag{24}$$

2.3. State-space model

Define the state vector x and the control vector u, as presented below

$$x=\begin{bmatrix}\theta\\ \dot{\theta}\\ x\\ \dot{x}\\ \delta\\ \dot{\delta}\end{bmatrix},\ u=\begin{bmatrix}T_L\\ T_R\end{bmatrix} \tag{25}$$

The solution function in MATLAB is used to calculate Eqs. (22)-(24), and the result of the system's nonlinear model is expressed as

$$\dot{x}=f\left(x,T_L,T_R\right) \tag{26}$$

The Jacobian function is then applied to linearize Eq. (26), and it yields

$$\dot{x}=Ax+Bu \tag{27}$$

The formulas for the Jacobian matrices at the equilibrium points of a nonlinear model are presented as

$$A=\frac{\partial f}{\partial x}(x,u)=\begin{bmatrix}0 & 1 & 0 & 0 & 0 & 0\\ A_{21} & 0 & 0 & 0 & 0 & 0\\ 0 & 0 & 0 & 1 & 0 & 0\\ A_{41} & 0 & 0 & 0 & 0 & 0\\ 0 & 0 & 0 & 0 & 0 & 1\\ 0 & 0 & 0 & 0 & 0 & 0\end{bmatrix} \tag{28}$$

$$B=\frac{\partial f}{\partial u}(x,u)=\begin{bmatrix}0 & 0\\ B_{21} & B_{22}\\ 0 & 0\\ B_{41} & B_{42}\\ 0 & 0\\ B_{61} & B_{62}\end{bmatrix} \tag{29}$$

From the value of state matrix A shown in Eq. (28) and Eq. (29), it can be seen that the four state variables about the straight-line control are not related to the two-state variables about the steering control.

2.4. Decoupling of the system

In order to reduce the influence of the straight-line controller on the steering controller, the objects of the control method are changed to the straight torque T_θ around the robot's axis and the steering torque T_δ around the z-axis. Therefore, it is

necessary to decouple the system before the system input, as shown in Fig. 4, to decouple the straight torque T_θ and steering torque T_δ into the left wheel torque T_L and the right wheel torque T_R [21].

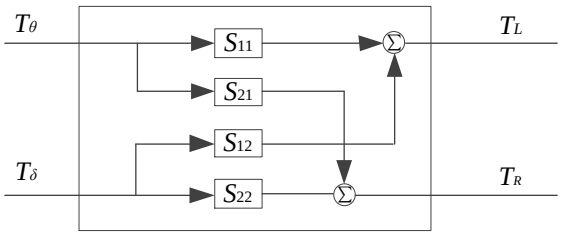

Fig. 4 System decoupling

Through the decoupling system in Fig. 4, the decoupling equation of the system can be obtained by

$$\begin{bmatrix} T_L \\ T_R \end{bmatrix} = \begin{bmatrix} S_{11} & S_{12} \\ S_{21} & S_{22} \end{bmatrix} \begin{bmatrix} T_\theta \\ T_\delta \end{bmatrix} \tag{30}$$

For the straight-line system, T_θ is used to control the robot's inclination θ and displacement x, and T_δ is employed to control the robot's steering angle δ. Substituting the decoupling equation into the state-space model shown in Eq. (27), the result is given by

$$\dot{x} = Ax + B'u' \tag{31}$$

$$u' = \begin{bmatrix} T_\theta \\ T_\delta \end{bmatrix} \tag{32}$$

$$B' = \begin{bmatrix} 0 & 0 \\ B_{21}S_{11} + B_{22}S_{21} & B_{21}S_{12} + B_{22}S_{22} \\ 0 & 0 \\ B_{41}S_{11} + B_{42}S_{21} & B_{41}S_{12} + B_{42}S_{22} \\ 0 & 0 \\ B_{61}S_{11} + B_{62}S_{21} & B_{61}S_{12} + B_{62}S_{22} \end{bmatrix} \tag{33}$$

The relationship between the four parameters of S_{11}, S_{12}, S_{21}, and S_{22} is fixed, but one of the quantities is arbitrarily valued, in this article S_{11} = 0.5, as presented below

$$\begin{bmatrix} T_L \\ T_R \end{bmatrix} = \begin{bmatrix} 0.5 & 0.5 \\ 0.5 & -0.5 \end{bmatrix} \begin{bmatrix} T_\theta \\ T_\delta \end{bmatrix} \tag{34}$$

After decoupling, the planar control system is divided into two independent subsystems, the straight control subsystem and the steering control subsystem. In the straight control subsystem, balance and speed are managed by the LQR controller, while the steering control subsystem is controlled by the PID controller.

3. Control

The structural block diagram of the robot's control system is shown in Fig. 5. The system's control comprises a height control system and a planar control system. In the height control system, the magnitude of the virtual force is adjusted through the PID controller, while the VMC controller is used to calculate the corresponding hip joint torque to control the robot's leg length. The decoupling system divides the planar control system of the wheeled inverted pendulum model into a straight control subsystem and a steering control subsystem, the LQR controller controls the system's straight-line motion and the PID controller adjusts its steering.

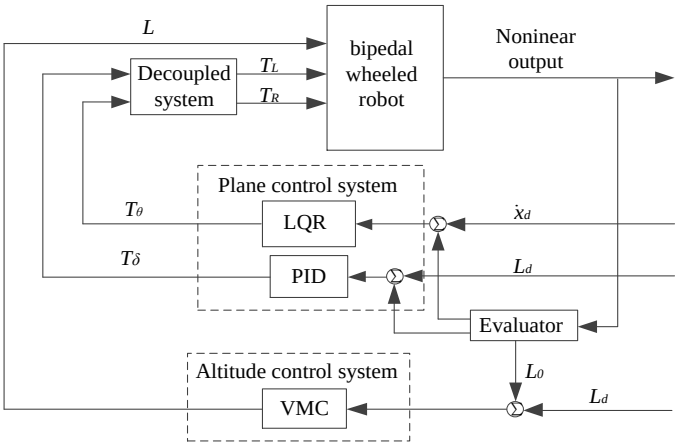

Fig. 5 Block diagram for the motion control system of a bipedal wheeled robot

3.1. LQR control

For the wheeled inverted pendulum model shown in Eq. (27), a feedback matrix K is applied to achieve optimal control, as presented below

$$u = K\left(x_d - x\right) = \begin{bmatrix} K_{11} & K_{12} & K_{13} & K_{14} & K_{15} & K_{16} \\ K_{21} & K_{22} & K_{23} & K_{24} & K_{25} & K_{26} \end{bmatrix} \left(\begin{bmatrix} 0 \\ 0 \\ 0 \\ \dot{x}_d \\ \delta_d \\ 0 \end{bmatrix} - \begin{bmatrix} \theta \\ \dot{\theta} \\ x \\ \dot{x} \\ \delta \\ \dot{\delta} \end{bmatrix} \right) \tag{35}$$

The feedback matrix K is calculated using LQR, and the cost function J is defined as follows

$$J = \int_0^{\infty} \left(x^T Q x + u^T R u \right) dt \tag{36}$$

where the weighting matrices question and response (Q and R) are used to balance the input and output weights. To minimize the cost function J, the output u, the feedback gain K and P should satisfy, respectively, the following equations

$$u = -R^{-1} B^T P x \tag{37}$$

$$K = R^{-1} B^T P \tag{38}$$

$$A^T P + PA - PAR^{-1} B^T P + Q = 0 \tag{39}$$

Considering the different leg lengths of the robot, linearization is performed every 10 mm within the leg length interval [22], and the corresponding feedback gain matrix K is calculated. For the variation of each element of the matrix with leg length L_0, the polynomial equation is fitted using the least squares method, and the polynomial equation is obtained by

$$K_{ij}\left(L_0\right) = p_{0|ij} + p_{1|ij} L_0 + p_{2|ij} L_0^2 \tag{40}$$

where p_0, p_1, and p_2 represent the coefficients of each term in the polynomial equation fitted.

In summary, the robot's feedback control rate is presented as follows

$$u = K_{ij}\left(L_0\right)\left(x_d - x\right) \tag{41}$$

3.2. VMC

Using the VMC approach, the virtual force F along the member AE is applied to the equivalent wheel-legged handstand pendulum model, and the hip moment T is outputted to achieve height control.

When the height of the robot is fixed, simple theoretical mechanics and statics are used to derive the following equation. To map forces or torques in the workspace to joint torques in joint space, it is necessary to establish the relationship between these two spaces, known as the forward kinematic model presented below. The principle of virtual work, can be expressed by

$$F\cos\theta_0 - \left(m_0 + 2m_1 + 2m_2 + 2m_{23} + 2m_3\right)g = 0 \tag{42}$$

$$x = f\left(q\right) \tag{43}$$

where $\boldsymbol{x} = L_0$ and $q = \theta_1$.

$$T^T \delta q + \left(-F\right)^T \delta x = 0 \tag{44}$$

Taking the full differential of Eq. (43) with respect to x, it yields

$$dx = \frac{dL_0}{dq_1} dq \tag{45}$$

and the Jacobian matrix J is defined as

$$J = \left[\frac{\delta L_0}{\delta \theta_1}\right] \tag{46}$$

Subsequently, substituting Eq. (46) into Eq. (45) yields Eq. (47). That is, the joint velocity δq is mapped to the attitude change rate δx of the four links by the Jacobian matrix.

$$\delta x = J\delta q \; T = J^T F \tag{47}$$

Consequently, substituting Eq. (47) with Eq. (44) gives Eq. (48).

$$T = J^T F \tag{48}$$

In summary, the hip moment can be solved by the Jacobian matrix of the forward kinematic model.

3.3. PID control

The mathematical expression for the PID controller can be obtained by

$$u\left(t\right) = K_p\left[e\left(t\right) + \frac{1}{K_i}\int_0^t e\left(t\right)dt + K_d\frac{de\left(t\right)}{dt}\right] \tag{49}$$

where $u(t)$ is the output of the controller, K_p is the proportional gain, K_i is the integral gain, and K_d is the derivative gain.

In the steering control system, the error between the expected yaw angle δ_d and the estimated yaw angle δ calculated by the attitude, that is δ_d-δ, obtains the steering torque output through the PID controller, and superimposes it into the straight torque, so as to obtain the left and right drive wheel motor torques.

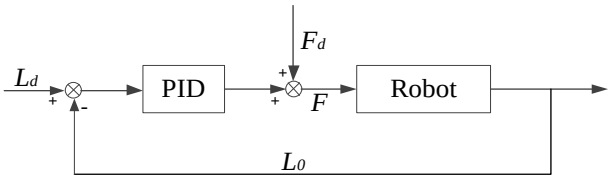

Fig. 6 PID-Feedforward control block diagram

In the leg length control system, the feedforward is used to compensate for the gravity of the robot body and legs, while the PID controller corrects the virtual force error of the feedforward model. The PID-Feedforward control block diagram is shown in Fig. 6, and the error between the expected leg length L_d and the actual leg length L_0, L_d-L_0 is calculated. The PID controller compensates for this error by generating a virtual force, which is then superimposed onto the static virtual force F_d, as presented as follows

$$F_d = \frac{\left(m_0 + 2m_1 + 2m_2 + 2m_{23} + 2m_3\right) g}{\cos\theta_0} \tag{50}$$

4. Simulation Testing

Table 3 Physical parameters of the robot

Symbols	Magnitude	Symbols	Magnitude
m	0.23(kg)	m_0	1.56(kg)
m_1	0.034(kg)	m_2	0.023(kg)
m_{23}	0.005(kg)	m_3	0.014(kg)
R	0.325(m)	D	0.246(m)
l_1	0.107(m)	l_2	0.108(m)
l_{23}	0.026(m)	l_3	0.111(m)
l_4	0.05(m)	g	9.8(m/s^2)

In order to verify the performance of the bipedal wheeled robot control method, simulation experiments are carried out in the Simulink module of MATLAB software. The physical parameters of the robot, shown in Table 3, are used to build a virtual model of the robot.

In the simulation test of the robot, the input leg length command controls the height of the robot, the input speed command controls the robot's forward motion, the yaw angle command controls the robot's steering, and the robot simulation starts from the near-ground falling position.

The key to designing an LQR optimal controller lies in the selection of the weighting matrices Q and R. The magnitude of the Q value is directly proportional to the system's disturbance rejection capability, but should not be excessively large. After multiple adjustments of the weighting matrices Q and R, the final selections can be obtained by

$$Q = \begin{bmatrix} 6000 & 0 & 0 & 0 & 0 & 0 \\ 0 & 1 & 0 & 0 & 0 & 0 \\ 0 & 0 & 1000 & 0 & 0 & 0 \\ 0 & 0 & 0 & 100 & 0 & 0 \\ 0 & 0 & 0 & 0 & 1000 & 0 \\ 0 & 0 & 0 & 0 & 0 & 1 \end{bmatrix}, R = \begin{bmatrix} 100 & 0 \\ 0 & 25 \end{bmatrix} \tag{51}$$

The corresponding feedback gain matrix K is calculated by the LQR function of MATLAB, and the Simulink control module is shown in Fig. 7.

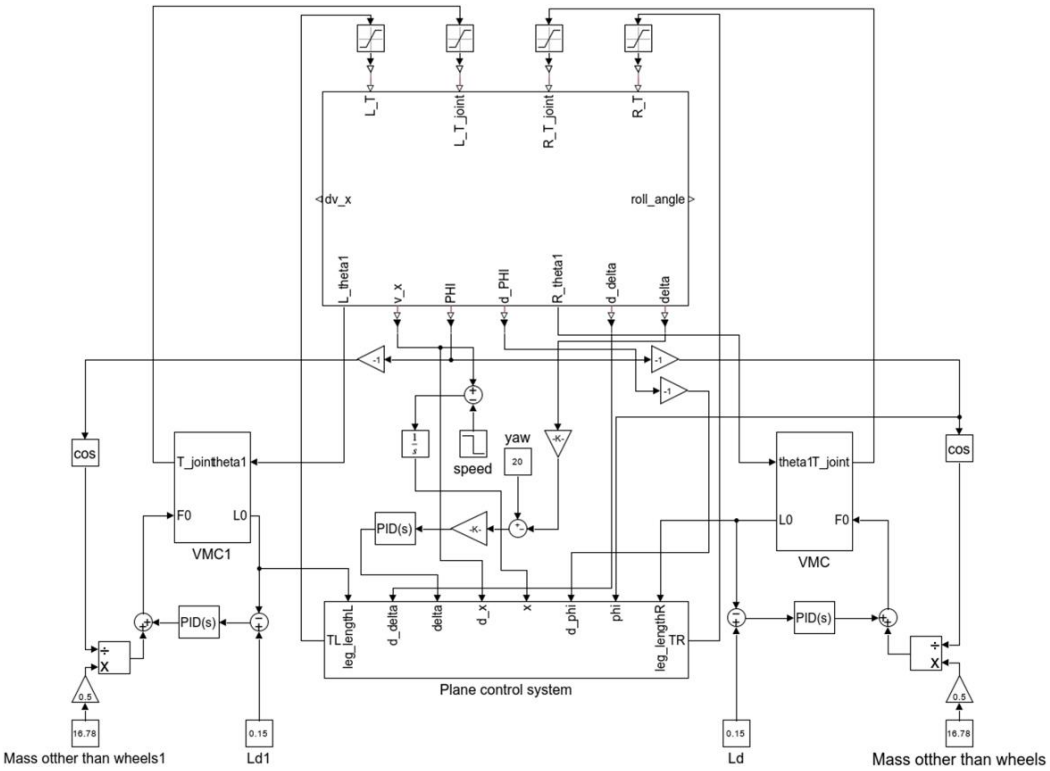

Fig. 7 Control module of a two-wheeled robot

4.1. Control performance at a fixed height

4.1.1. Simulation of an autonomous balanced state

According to different needs and working conditions, a robot motion control test under decoupling conditions is carried out to analyze its stability, straight-line control, and steering performance. The initial conditions are set as follows: the expected leg length (leg length in the patrol state) L_d is 0.15 m, the expected yaw angle d_d is 20°, and the expected velocity is specified as follows

$$\dot{x}_d\left(^m/_s\right)=\begin{cases}2, & t<5\\ 0, & t\geq 5\end{cases} \tag{52}$$

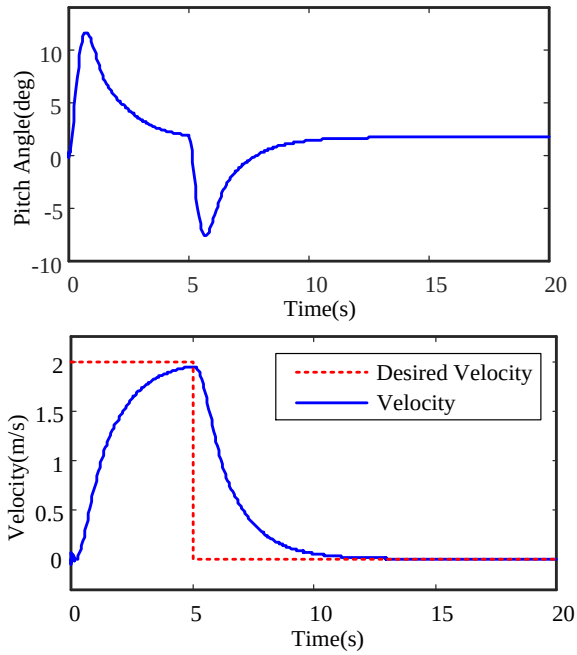

Fig. 8 LQR balance disturbance simulation results

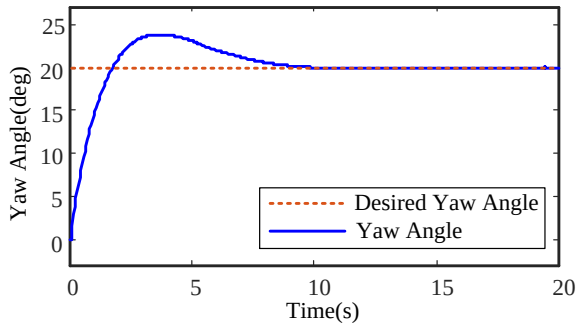

Fig. 8 LQR balance disturbance simulation results (continued)

Fig. 8 illustrates that the system reaches a steady state after approximately 11 seconds of adjustment, with both velocity and yaw angle achieving their expected values.

4.1.2. The system equilibrium state is disturbed simulation

First, the initial parameters of the system should be consistent with those in the autonomous balanced state. An external input step signal lasting 1 second simulates an unbalanced scenario where the system is disturbed. The test results are shown in Fig. 9.

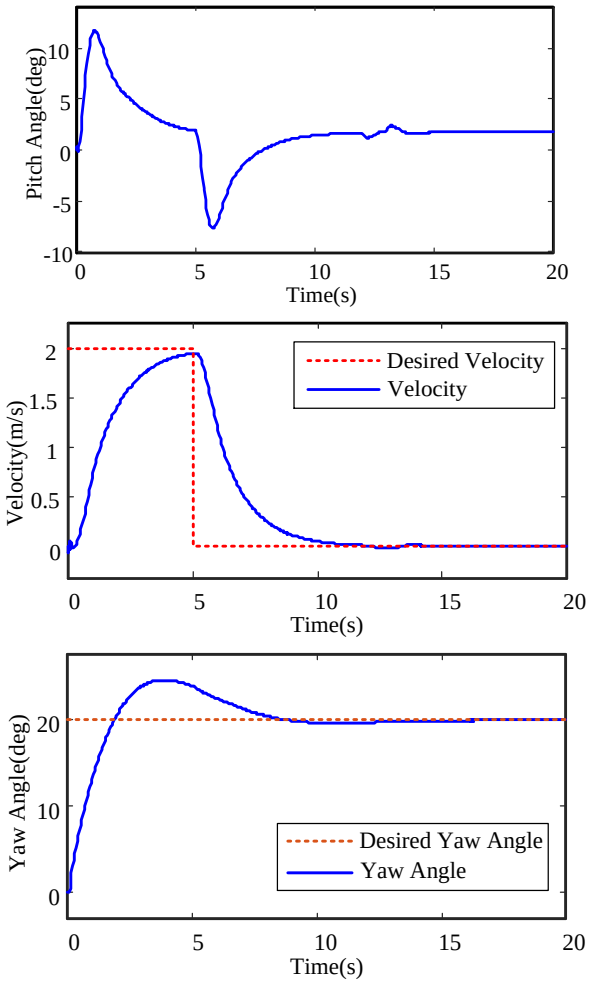

Fig. 9 LQR balance disturbance simulation results

As can be seen from Fig. 9, after applying disturbances that disrupt the equilibrium state, there is a significant variation in the pitch angle of the system. However, the system is able to autonomously return to equilibrium within a short period, and the overshoot of the system remains within permissible limits. It can be seen that the LQR controller satisfies the disturbance rejection requirements under these conditions.

4.2. Control performance at variable height

Table 4 Simulation parameters 1

	L_d (m)	$\dot{x}_d$ (m/s)	δ_d (°)
Squatting	0.08	$\begin{cases} 2, & t<5 \\ 0, & t\geq 5 \end{cases}$	0
Standing	0.18	$\begin{cases} 2, & t<5 \\ 0, & t\geq 5 \end{cases}$	0

When the robot assumes squatting and standing postures, it is at different heights, as depicted in Fig. 10. The left side of Fig. 10 illustrates the robot's equilibrium state with a leg height L_d = 0.08 m, while the right side shows the equilibrium state with a leg height L_d = 0.18 m. The initial conditions of the robot at variable height are presented in Table 4. Fig. 11 displays the control performance of the robotic system during forward movement in both crouching and standing states, achieving stability at varying heights.

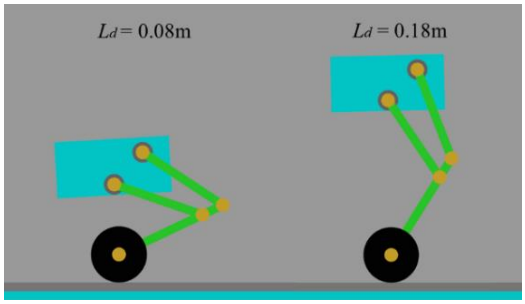

Fig. 10 The robot is in two states: squatting and standing

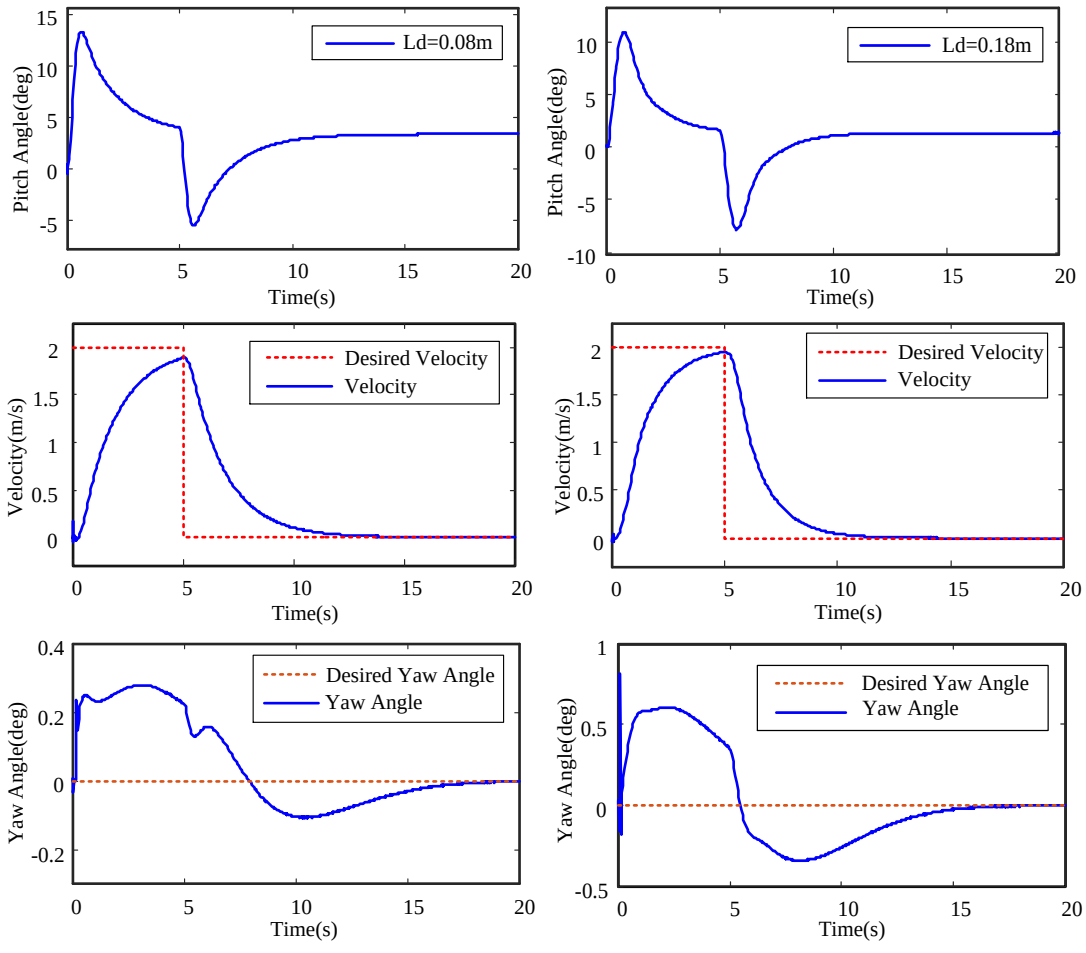

Fig. 11 Squatting-standing simulation test renderings (squatting on the left, standing on the right)

4.3. Decoupling-coupling simulation performance test

Table 5 Simulation parameters 2

	L_d (m)	$\dot{x}_d$ (m/s)	δ_d (°)
Decoupling	0.15	$\begin{cases} 2, & t<5 \\ 0, & t\geq 5 \end{cases}$	20
Coupling	0.15	$\begin{cases} 2, & t<5 \\ 0, & t\geq 5 \end{cases}$	20

To investigate the impact of a decoupling system on the balance and steering performance of the robot, under the condition that the expected leg length, the expected velocity, and the expected yaw angle are the same, as shown in Table 5, the robot control system with and without a decoupling system is simulated and compared. Fig. 12 demonstrates that the decoupling system provides slight improvements in the balance performance of the robot while also accelerating the convergence speed of the yaw angle with reduced overshoot.

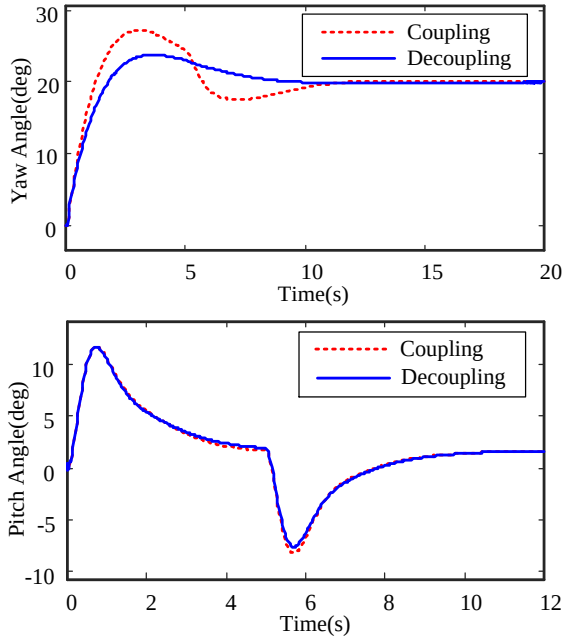

Fig. 12 Comparison of decoupling-coupling simulations

5. Conclusion

In this study, the wheeled inverted pendulum model of the bipedal wheeled robot which is equivalent to the legs-airframe centroid variable rod is linearized and decoupled, and the straight-line control subsystem and steering control subsystem are obtained. The straight-line control subsystem employs LQR control, while the steering control subsystem utilizes PID control. In the robot's height control system, the method of PID-Feedforward is used to adjust the magnitude of the virtual force, while VMC is introduced to solve the hip moment to achieve height control. In MATLAB, a simulation platform for the robot was built to test the performance of the proposed control system.

(1) Through MATLAB simulations, the feasibility of the LQR and VMC algorithms for the bipedal wheeled robot is validated, enabling precise control over the robot's leg height and facilitating obstacle avoidance in complex environments.

(2) By comparing the simulation results of the robot control systems with and without a decoupling system, it is observed that the decoupling system provides slight improvements in the robot's balance performance, and accelerates the convergence speed of the yaw angle with reduced overshoot.

Due to the limitations of the robot's positioning, the jumping function of the robot is not analyzed in this study. In future research on the jumping function of this type of robot, a nonlinear spring virtual model will be derived based on the analysis of the robot's in-place leg hopping [23]. The wheel control algorithm based on the aerial dynamics model enables the robot to be controllable in the air, thereby realizing the robot's jumping function.

Due to limitations of the LQR algorithm, the values of the weighting matrices Q and R are suboptimal, and the algorithm employed in this study fails to address system disturbances. In future research aimed at improving the algorithm proposed in this study, the Newton-Raphson method will be utilized to adjust the weighting matrices Q and R [24], and fuzzy algorithms will be introduced to enhance the system's resistance to disturbances.

Acknowledgments

This research was supported by a Graduate practice innovation project of the Yancheng Institute of Technology, under Grant SJCX23_XZ007. We thank Wei Yin, a Postgraduate for assistance with the balance control algorithms by LQR, and Jian Chen, a teacher, at the Yancheng Institute of Technology for comments that greatly improved the manuscript.

Conflicts of Interest

The authors declare no conflict of interest.

References

[1] M. H. Korayem, M. Safarbali, and N. Y. Lademakhi, "Adaptive Robust Control with Slipping Parameters Estimation Based on Intelligent Learning for Wheeled Mobile Robot," ISA transactions, vol. 147, pp. 577-589, 2024.

[2] J. A. Rodríguez-Arellano, R. Miranda-Colorado, L. T. Aguilar, and M. A. Negrete-Villanueva, "Trajectory Tracking Nonlinear H∞ Controller for Wheeled Mobile Robots with Disturbances Observer," ISA transactions, vol. 142, pp. 372-385, 2023.

[3] Y. H. Pham, T. L. Nguyen, T. T. Bui, and T. V. Nguyen, "Adaptive Active Fault Tolerant Control for a Wheeled Mobile Robot under Actuator Fault and Dead Zone," IFAC-PapersOnLine, vol. 55, no. 37, pp. 314-319, 2022.

[4] J. P. Kolhe, S. Soumya, and S. E. Talole, "Disturbance Estimation based Robust Center of Mass Tracking Control of Humanoid Robot," IFAC-PapersOnLine, vol. 57, pp. 315-320, 2024.

[5] P. Ferrari, L. Rossini, F. Ruscelli, A. Laurenzi, G. Oriolo, N. G. Tsagarakiset, et al., "Multi-Contact Planning and Control for Humanoid Robots: Design and Validation of a Complete Framework," Robotics and Autonomous Systems, vol. 166, article no. 104448, 2023.

[6] J. N. Nganga, H. Li, and P. M. Wensing, "Second-Order Differential Dynamic Programming for Whole-Body MPC of Legged Robots," IFAC-PapersOnLine, vol. 56, no. 3, pp. 499-504, 2023.

[7] J. Dong, R. Liu, B. Lu, X. Guo, and H. Liu, "LQR-Based Balance Control of Two-Wheeled Legged Robot," 41st Chinese Control Conference, pp. 450-455, 2022.

[8] L. Zhao, Z. Yu, X. Chen, G. Huang, W. Wang, L. Han, et al., "System Design and Balance Control of a Novel Electrically-Driven Wheel-Legged Humanoid Robot," IEEE International Conference on Unmanned Systems, pp. 742-747, 2021.

[9] J. Zhang, Z. Li, S. Wang, Y. Dai, R. Zhang, J. Lai, et al., "Adaptive Optimal Output Regulation for Wheel-Legged Robot Ollie: A Data-Driven Approach," Frontiers in Neurorobotics, vol. 16, article no. 1102259, 2022.

[10] X. Liu, Y. Sun, S. Wen, K. Cao, Q. Qi, X. Zhang, et al., "Development of Wheel-Legged Biped Robots: A Review," Journal of Bionic Engineering, vol. 21, no. 2, pp. 607-634, 2024.

[11] L. Cui, S. Wang, J. Zhang, D. Zhang, J. Lai, Y. Zheng, et al., "Learning-Based Balance Control of Wheel-Legged Robots," IEEE Robotics and Automation Letters, vol. 6, no. 4, pp. 7667-7674, 2021.

[12] S. Wang, L. Cui, J. Zhang, J. Lai, D. Zhang, K. Chen, et al., "Balance Control of a Novel Wheel-Legged Robot: Design and Experiments," IEEE International Conference on Robotics and Automation, pp. 6782-6788, 2021.

[13] C. F. Hsu, B. R. Chen, and Z. L. Lin, "Implementation and Control of a Wheeled Bipedal Robot Using a Fuzzy Logic Approach," Actuators, vol. 11, no. 12, article no. 11120357, 2022.

[14] H. Cao, B. Lu, H. Liu, R. Liu, and X. Guo, "Modeling and MPC-Based Balance Control for a Wheeled Bipedal Robot," 41st Chinese Control Conference, pp. 420-425, 2022.

[15] J. Zhang, S. Wang, H. Wang, J. Lai, Z. Bing, Y. Jiang, et al., "An Adaptive Approach to Whole-Body Balance Control of Wheel-Bipedal Robot Ollie," IEEE/RSJ International Conference on Intelligent Robots and Systems, pp. 12835-12842, 2022.

[16] A. Kanungo, C. Choubey, V. Gupta, P. Kumar, and N. Kumar, "Design of an Intelligent Wavelet-Based Fuzzy Adaptive PID Control for Brushless Motor," Multimedia Tools and Applications, vol. 82, no. 21, pp.33203-33223, 2023.

[17] A. Kanungo, M. Mittal, L. Dewan, V. Mittal, and V. Gupta, "Speed Control of DC Motor with MRPID Controller in the Presence of Noise," Wireless Personal Communications," vol. 124, pp. 893-907, 2022.

[18] M. A. I. Filho, E. Puchta, M. S. R. Martins, T. A. Alves, Y. D. S. Tadano, F. C. Corrêa, et al., "Bio-Inspired Optimization Algorithms Applied to the GAPID Control of a Buck Converter," Energies, vol. 15, no. 18, article no. 6788, 2022.

[19] Y. Shao, J. Liu, J. Huang, L. Hu, L. Guo, and Y. Fang, "The Implementation of Fuzzy PSO-PID Adaptive Controller in Pitch Regulation for Wind Turbines Suppressing Multi-Factor Disturbances," Frontiers in Energy Research, vol. 9, article no. 828281, 2022.

[20] J. Yuan, H. Chen, T. Yong, X. Lai, and X. Chen, "Research on Two-Wheeled Balance Car Based on Improved LQR Controller," IEEE 6th Advanced Information Technology, Electronic and Automation Control Conference, pp. 1474-1479, 2022.

[21] L. Guo, S. A. A. Rizvi, and Z. Lin, "Optimal Control of a Two-Wheeled Self-Balancing Robot by Reinforcement Learning," International Journal of Robust and Nonlinear Control, vol. 31, no. 6, pp. 1885-1904, 2021.

[22] X. Feng, S. Liu, Q. Yuan, J. Xiao, and D. Zhao, "Research on Wheel-legged Robot Based on LQR and ADRC," Scientific Reports, vol. 13, article no. 15122, 2023.

[23] T. Guo, J. Liu, H. Liang, Y. Zhang, W. Chen, X. Xia, et al., "Design and Dynamic Analysis of Jumping Wheel-Legged Robot in Complex Terrain Environment," Frontiers in Neurorobotics, vol. 16, article no. 1066714, 2022.

[24] S. J. Chacko, and R. J. Abraham, "On LQR Controller Design for an Inverted Pendulum Stabilization," International Journal of Dynamics and Control, vol. 11, no. 4, pp. 1584-1592, 2023.